Impact of Process Conditions on the Properties of Additively Manufactured Tool Steel H13 processed by LBM

L. Wu, T.Klaas, S. Leuders, F. Brenne, T. Niendorf

H13 tool steel, a versatile chromium hot-work steel, is widely used in demanding industrial applications such as high-pressure die casting. When processed by additive manufacturing (AM), innovative functionalities like conformal cooling can be implemented in these tools in order to optimize the thermal management as well as the linked processing cycle time. However, due to the high carbon content, robust processing of H13 requires high pre-heating temperatures, which cannot be achieved by many commonly available Laser beam melting (LBM) systems. This could be different for the Electron beam melting (EBM) process, where pre-heating temperatures of more than 1000 °C can be achieved. Against this background, the present study provides a first step towards process parameter development for H13 tool steel. For H13 processed by LBM it is shown that application relevant material characteristics, such as defect-density, surface quality and mechanical properties, are strongly influenced by the processing parameters.

KEYWORDS: HOT WORK STEEL H13, LASER BEAM MELTING, LASER PARAMETER, MELTING POOL, SOLIDIFICATION CRACKS

INTRODUCTION

During recent years, the field of additive manufacturing (AM) gained steadily growing interest from industry and academia due to its outstanding potentials, i.e. design freedom, light-weight design, realization of complex inner structures, etc.[1]. In recent decades, different AM technologies were established and improved, while numerous materials were processed. Two well-established methods of AM, Laser beam melting (LBM) and Electron beam melting (EBM) are under consideration in the current work. Although the basic principle is similar, i.e. layer-wise manufacturing from a powder bed, LBM and EBM have some differences, which are listed in Tab.1.

Tab. 1 – List of differences between LBM and EBM

Difference	LBM	EBM
Source	Laser beam	Electron beam
Powder	Fine	Coarse
Vacuum	no	yes

H13 is a commercial hot-work steel. The standard composition (according to DIN standard) is listed in Tab.2. Recent investigations show that H13 in general can be processed by AM [2-4]. Studies focused on effect of pre-heating and processing windows on porosity and monotonic properties (cf. Fig.1) however, solid process-microstructure-property relationships allowing transfer of results to other AM facilities are not established so far.

L. Wu, T.Klaas, S. Leuders
Voestalpine Additive Manufacturing Center GmbH,
Hansaallee 321, 40549 Düsseldorf, Germany

F. Brenne, T. Niendorf
Institut für Werkstofftechnik (Materials Engineering),
Mönchebergstr. 3, 34125 Kassel, Germany

Tab. 2– Nominal chemical composition of H13 steel [4]

Elements	C	Si	Mn	Cr	Mo	V	Fe
wt.%	0.35-0.42	0.80-1.20	0.25-0.50	4.80-5.50	1.20-1.50	0.90-1.10	Bal.

Analysis of the melting pool, i.e. its morphology and dimensions, provides a first step towards understanding of the impact of processing parameters on microstructure and defect evolution for both, LBM and EBM. Thus, melting pool analyses could provide the basis for process parameter development in a joint fashion for both techniques. The current study reveals the impact of three parameters for one technique (LBM) only, studies focusing on EBM will be future work.

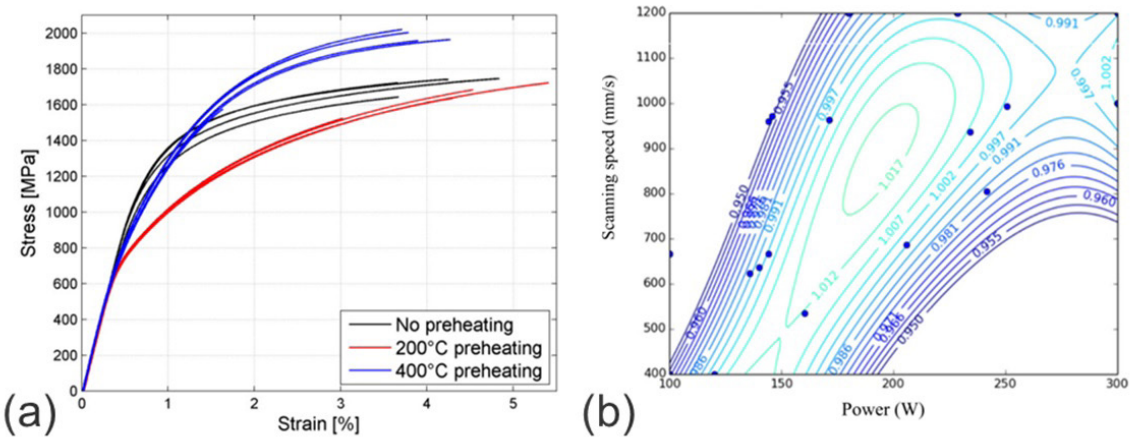

Fig. 1 – (a) Stress strain curves for samples without, with 200°C and with 400°C preheating [3] (b) Density contour plot as a function of scan speed and power [2]

Experimental details

For this study, specimens have been processed under an argon gas atmosphere on a SLM 280HL machine (SLM Solutions GmbH) equipped with a high-temperature (HT) heating stage, employing an yttrium fiber laser with a maximum power of 700 W. The layer thickness was set to 30 µm and the platform was heated to 200 °C, 300°C and 400°C. As raw material, gas-atomized H13 has been used. Detailed information on the powder is provided in Tab.3.

Tab. 3 – H13 powder used in the current study

Elements	C	Si	Mn	Cr	Mo	V	Fe
wt.%	0.37	0.97	0.58	5.24	1.74	1.16	Bal.
Size distribution		D10		D50		D90	
µm		18.2		28.5		43.5	

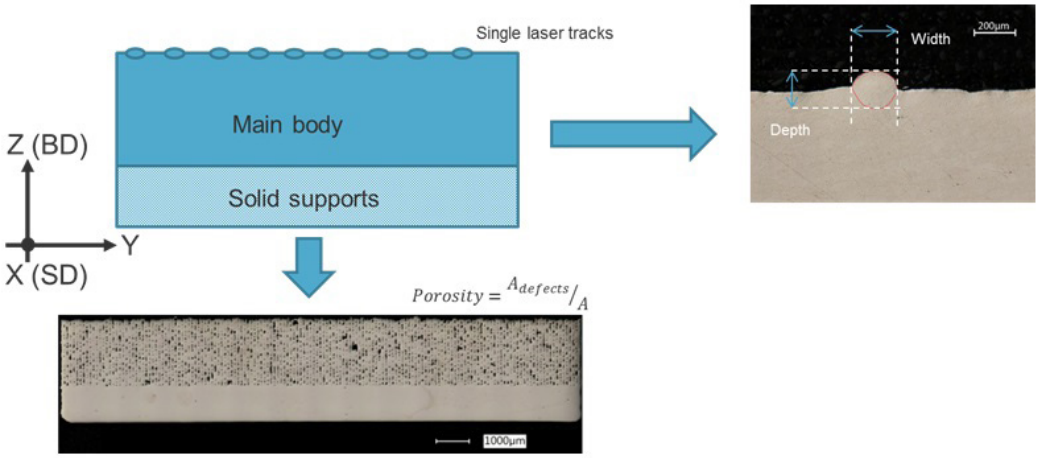

Fig. 2 – Design of specimens: single laser tracks for melting pool analysis and bulk material for porosity analysis

For the investigation of melting pools and porosity using different parameters, specimen were designed as depicted in Fig.2. Using the SLM process, the specimens were built in z-direction and single laser tracks were scanned back and forth in x-direction. In order to investigate the influence of parameters, 3 x 9 specimens at temperatures of 200 °C, 300°C and 400°C were conducted according to Tab.4.

Tab. 4 – Parameter setting for 9 specimens at temperatures of 200 °C, 300°C and 400°C

Nr.	1	2	3
Laser Power (W)	100	200	300
Scan speed (mm/s)	450	450	450
Hatch distance (mm)	0.1	0.1	0.1
Nr.	4	5	6
Laser Power (W)	100	200	300
Scan speed (mm/s)	900	900	900
Hatch distance (mm)	0.1	0.1	0.1
Nr.	7	8	9
Laser Power (W)	100	200	300
Scan speed (mm/s)	1350	1350	1350
Hatch distance (mm)	0.1	0.1	0.1

For characterization, all specimens were cut in the y-z section, mechanically ground and polished, and etched by Nital 3%. For optical microscopy a digital microscopy Keyence VHX-5000 was used. Quantification of porosity and analyses of melting pools was conducted based on optical micrographs. Additionally, microstructure was characterized by scanning electron microscopy (SEM) employing a JEOL JSM-IT 300.

RESULTS AND DISCUSSION

As mentioned in the experimental details section, 27 different specimens were built in total. Information on porosity and melting pool dimensions are provided in Tab.5.

Tab. 5 – Porosity and melting pool dimensions

T(°C)	No.	Power(W)	Speed(mm/s)	Porosity (%)	Melting pool	
					Width(μm)	Depth(μm)
200	1	100	450	0.47	116.19	76.50
	2	200	450	0.02	167.95	156.70
	3	300	450	0.01	191.01	111.23
	4	100	900	5.28	97.47	74.82
	5	200	900	0.03	115.25	72.19
	6	300	900	0.09	158.36	94.03
	7	100	1350	29.39	78.11	64.96
	8	200	1350	3.75	94.86	72.08
	9	300	1350	0.42	105.28	96.23
300	1	100	450	0.43	99.34	75.75
	2	200	450	0.01	149.00	116.81
	3	300	450	0.02	188.33	137.60
	4	100	900	9.68	84.96	60.98
	5	200	900	0.04	122.07	127.00
	6	300	900	0.05	116.06	90.41
	7	100	1350	26.91	83.15	62.97
	8	200	1350	2.71	107.15	92.48
	9	300	1350	0.06	116.65	84.81
400	1	100	450	0.27	114.32	77.06
	2	200	450	0.23	115.84	75.39
	3	300	450	0.01	200.78	166.90
	4	100	900	8.12	84.92	68.80
	5	200	900	0.01	125.50	113.82
	6	300	900	0.10	134.04	154.33
	7	100	1350	25.39	80.62	57.86
	8	200	1350	2.02	94.02	61.85
	9	300	1350	0.10	120.95	82.97

In order to analyze the interaction of various parameters on melt pool dimensions and evolution of porosity, Minitab 17 was applied to do the DoE analysis.
Fig. 3 (a) and (b) reflect the influence of laser power, scan speed and temperature on the width of the melting pools. The factor temperature does have only minor influence, the width of the melting pool is stronger influenced by laser power and scan speed. Similarly, the depth of the melting pools is affected. Fig.4 (a) and (b) reveal the same tendencies as Figure 3.

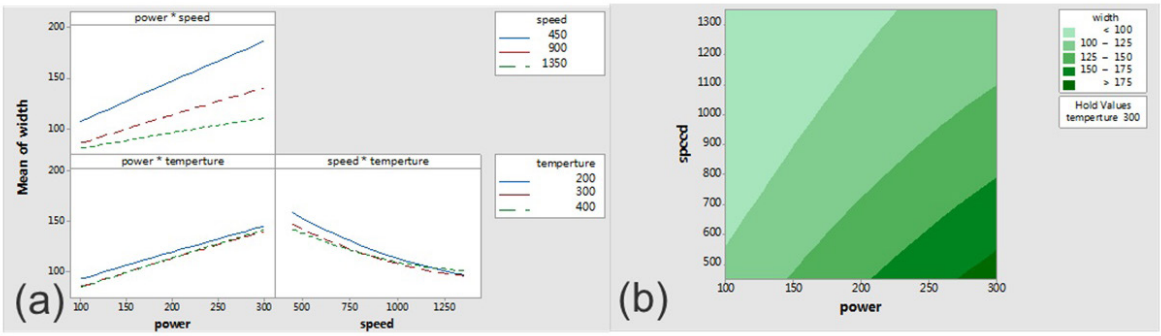

Fig. 3 – Influence of power, speed and temperature on the width of melting pools. (a) Interaction of main factors (b) contour plot for factors power and speed at 300°C

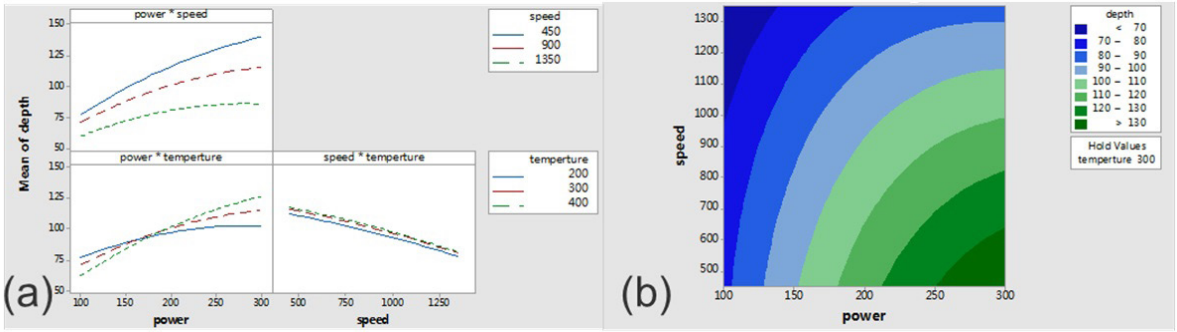

Fig. 4 – Influence of power, speed and temperature on the depth of melting pools. (a) Interaction of main factors (b) contour plot for factors power and speed at 300°C

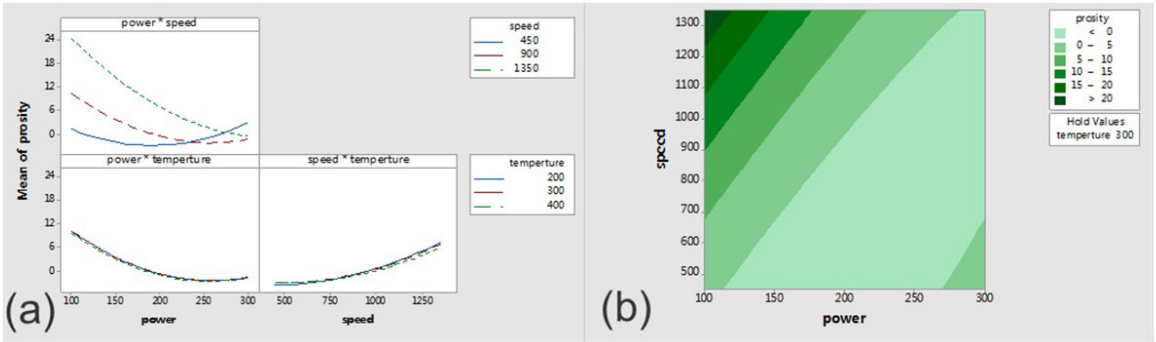

Fig. 5 – Influence of power, speed and temperature on the porosity. (a) Interaction of main factors (b) contour plot for factors power and speed at 300°C

The decrease of scan speed and the increase of power results in the reduction of porosity in large parts of the investigated range as highlighted in Fig.5. This phenomenon indicates that porosity is strongly affected by width and depth of the melt pool in the parameter range investigated.
The relationship between melting pool dimensions and porosity can be reflected not only from the data presented above, but also from metallographic analyses. Fig. 6 (a), (b) and (c) display optical micrographs from specimen processed with different parameters. With increasing power melting pools enlarge and pores surrounding melting pools gradually shrink and finally disappear. Furthermore, defects can be classified into two types, i.e. inside and surrounding melting pools.
Typical defects surrounding melting pools are pores, which are mostly filled with unmolten powder. Fig.7 (a) and (b) display the morphology of pores in the SEM and a corresponding schematic view. Obviously, the junctions of melting pools show high risk for evolution of pores. The schematic depicted in Fig.7 (c) provides a simple description of the underlying mechanism. Obviously, melting pool dimensions have to be set according to hatch distance and layer thickness to avoid this effect.

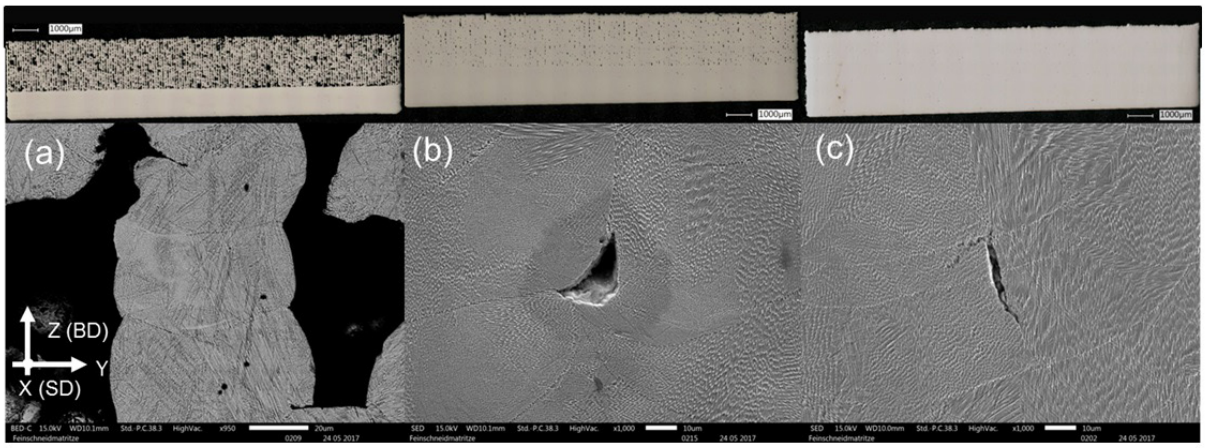

Fig. 6 – Melting pools and porosity upon LBM with different parameters (speed 1350mm/s, hatch 0.1mm, temperature 300°C are constant) (a) power 100W, (b) power 200W, (c) power 300W

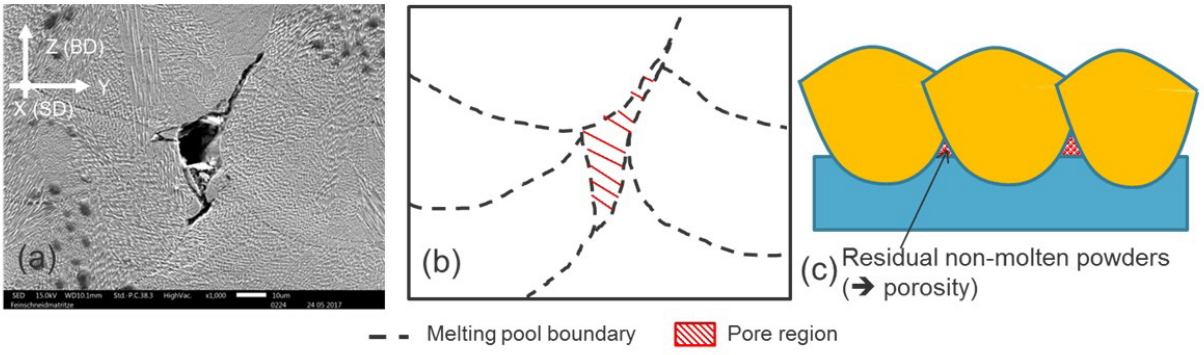

Fig. 7 – Pores surrounding melting pools (a) morphology of pores as seen in the SEM (b) schematic related to the SEM image (c) schematic description of mechanism leading to porosity

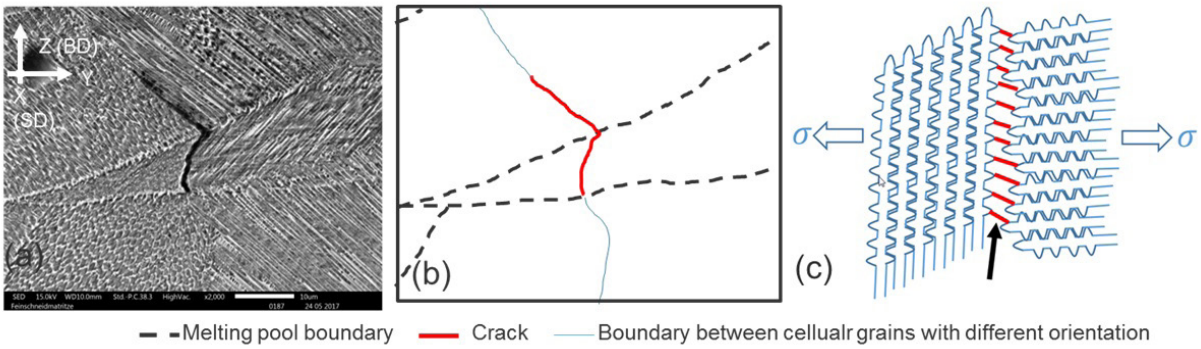

Fig. 8 – Cracks inside melting pools (a) morphology of cracks in SEM (b) schematic related to the SEM image (c) schematic highlighting the mechanism of solidification cracking [5, 6]

Inside the melting pools, another type of cracks is frequently observed. Fig.8 (a) and (b) show that cellular and elongated structures accompanied by cracks can be seen in individual grains. The type of cracks seen initiates and grows alongside the boundaries of clusters of similar appearance, even across boundaries of melting pools. According to literature [5, 6], these cracks are assumed to be solidification cracks, which form primarily on high-angle grain boundaries (HAGBs) and result from segregation of critical elements. Fig.8 (c) depicts schematically the mechanism responsible for crack formation. Detailed analyses, however, will be done in future work and focus on local grain orientations and character of grain boundaries.

Although porosity can be significantly reduced by increase of melting pool dimensions in the region investigated (at constant hatch distance and layer thickness), too high volume energy density (VED) is detrimental.

Fig.9 (a) and (b) display morphology and microstructure of a high VED specimen (power 500W, speed 450mm/s, hatch distance 0.1mm) in the y-z section. Cracks particularly evolve within the large melting pools (red boxes in Figure 9 (a)), simultaneously coarse dendrite structures evolve as can be seen in the SEM micrograph. This kind of solidification structure is strongly influenced by prevailing thermal gradients and growth rate of the solidification front (Fig.9 (c)). For AM, high-power LBM could speed up the manufacturing process. However, the specimens are more susceptible to cracks, non-favorable microstructure, high evaporation etc.

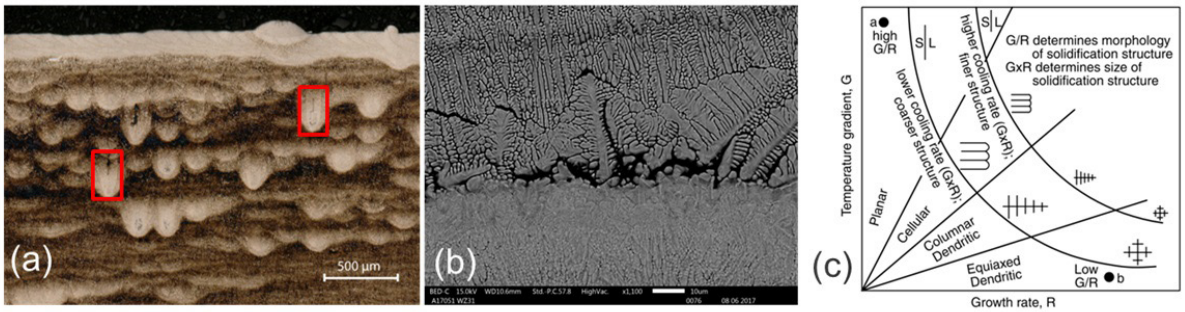

Fig. 9 – High-power LBM specimens, (a) morphology (b) microstructure obtained by SEM (c) influence of G and R on microstructure [7]

CONCLUSIONS

The current study focused on the influence of the three processing parameters (laser power, scan speed and temperature) in LBM on melting pool dimensions and porosity for hot-work steel H13. The following conclusions can be drawn:

1. In the investigated process parameter region, porosity of specimens decreases when laser power increases and scan speed decreases. This is due to an increase of width and depth of the melting pools.
2. Pores and cracks detected highlight the important role of melting pool dimensions. Porosity is caused by an unsuitable arrangement of melting pool dimensions, hatch distance and layer thickness.
3. Cracks located inside of melting pools follow grain boundaries. Solidification cracking is expected to be affected by segregation of critical elements.
4. High energy density LBM causes more intense cracking, inappropriate microstructure evolution and evaporation of elements.

REFERENCES

[1] Schmidt, V. and M.R. Belegratis, Laser technology in biomimetics: Basics and applications. 2014: Springer Science & Business Media.

[2] Laakso, P., et al., Optimization and Simulation of SLM Process for High Density H13 Tool Steel Parts. Physics Procedia, 2016. 83: p. 26-35.

[3] Mertens, R., et al., Influence of Powder Bed Preheating on Microstructure and Mechanical Properties of H13 Tool Steel SLM Parts. Physics Procedia, 2016. 83: p. 882-890.

[4] Papageorgiou, D., C. Medrea, and N. Kyriakou, Failure analysis of H13 working die used in plastic injection moulding. Engineering Failure Analysis, 2013. 35: p. 355-359.

[5] Lu, L., D. Raabe, and W. Bleck, Characterization of the crack formation mechanism in Ni-based superalloy Inconel 738LC produced by Selective Laser Melting (SLM). 2015, Institut für Eisenhüttenkunde, RWTH Aachen Aachen, Germany.

[6] Wang, N., et al., Solidification cracking of superalloy single-and bi-crystals. Acta Materialia, 2004. 52(11): p. 3173-3182.

[7] Kou, S., Welding metallurgy. New York, 1987.